ARTICLE IN PRESS
JID: JMAA [m5+;February 17, 2022;13:51]

Available online at www.sciencedirect.com

ScienceDirect

Journal of Magnesium and Alloys xxx (xxxx) xxx

www.elsevier.com/locate/jma

Full Length Article

Development and experimental validation of kinetic models for the hydrogenation/dehydrogenation of Mg/Al based metal waste for energy storage

M. Passing[a], C. Pistidda[a,*], G. Capurso[a], J. Jepsen[a,b], O. Metz[a], M. Dornheim[a], T. Klassen[a,b]

[a] *Institute of Hydrogen Technology, Helmholtz-Zentrum Hereon, Max-Planck-Straße 1 D, Geestacht 21502, Germany*
[b] *Institute of Materials Technology, Helmut Schmidt University, Holstenhofweg 85 D, Hamburg 22043, Germany*

Received 20 September 2021; received in revised form 12 November 2021; accepted 10 December 2021
Available online xxx

Abstract

With the increased use of renewable energy sources, the need to store large amounts of energy will become increasingly important in the near future. A cost efficient possibility is to use the reaction of recycled Mg waste with hydrogen as thermo-chemical energy storage. Owing to the high reaction enthalpy, the moderate pressure and appropriate temperature conditions, the broad abundance and the recyclability, the Mg/Al alloy is perfectly suitable for this purpose. As further development of a previous work, in which the performance of recycled Mg/Al waste was presented, a kinetic model for hydro- and dehydrogenation is derived in this study. Temperature and pressure dependencies are determined, as well as the rate limiting step of the reaction. First experiments are carried out in an autoclave with a scaled-up powder mass, which is also used to validate the model by simulating the geometry with the scaled-up experiments at different conditions.

Keywords: Thermo-chemical energy storage; Hydrogen storage; Metal hydride; Magnesium based waste; Recycling.

1. Introduction

In the last decades, the awareness of the influence of greenhouse gasses on the climate grew significantly [1]. This led the European council in 2018 to approve unprecedentedly strict regulations aiming at reducing greenhouse gas emissions in the European area [2]. The goal of these regulations is to keep the average temperature rise (*i.e.* global warming) well below 2 °C compared to the pre-industrial level.

To achieve this goal, a swift shift from fossil fuels to renewable energy sources is mandatory. Due to their intermittent nature and uneven distribution on earth, the exploitation of the energy produced by renewable sources is challenging. In this scenario, the development of energy storage systems that allow an efficient and synergic exploitation of these energy sources is of primary importance.

Hydrogen is considered as one of the most attractive future energy carriers [3]. Hydrogen possess a gravimetric energy density (*i.e.* 33.3 kWh/kg_{H2}) that is higher than those of common fossil fuels, like natural gas (*i.e.* 13.9 kWh/kg) or gasoline (*i.e.* 11.5 kWh/kg) [4]. Unfortunately, due to its low specific weight, the volumetric energy density of hydrogen is relatively poor even when compressed (*i.e.* 1.3 kWh/l at 700 bar and ambient temperature) and or liquefied (*i.e.* 2.3 kWh/l at 2 bar and −253 °C), compared to the value of 8.8 kWh/l of gasoline [4].

Owing to the high-energy storage densities achievable by storing hydrogen in solid-state, metal hydrides have been intensively investigated as potential hydrogen storage media for mobile and stationary applications [5–7]. Moreover, the possibility to employ this class of materials, for heat storage purposes has been also probed. In fact, the so called “high temperature metal hydrides” (*e.g.* CaH_2, LiH, MgH_2, *etc.*) are characterized by chemical reactions with heat storage capacities that are largely higher than those of the sensible heat from

* Corresponding author.
E-mail address: claudio.pistidda@hereon.de (C. Pistidda).

https://doi.org/10.1016/j.jma.2021.12.005

Table 1
Comparison of different storage materials regarding the gravimetric and volumetric energy density as well as the specific costs as listed in [29,30].

Storage material	Gravimetric energy density kJ/kg	Volumetric energy density MJ/m^3	Specific cost €/kg	Refs.
Nitrate-based				
60 $NaNO_3$: 40 KNO_3	491	901	1.13	[31]
$LiNaKCaNO_3$	542	977	0.61	[32]
Chloride-based				
KMgCl	271	431	0.3	[33]
NaMgCaCl	289	740	0.15	[34]
Fluoride-based				
LiNaKF	391	824	1.73	[34]
NaBF	474	885	4.23	[35]
Carbonate-based				
$MgCO_3$	1147	3396	0.43	[29]
LiF-$NaKCO_3$	843	1777	1.75	[30,36]
Hydride-based				
CaH_2	3857	6557	5.20	[29]
MgH2	2811	3995	2.34	[29]
Waste Mg/Al hydride	2146	3340	0.3–0.9*	This work

* Estimated according to the current available cost level of aluminum scrap and the cost ratio between primary aluminum to primary magnesium of about 5–10% higher prices of Mg [37].

commonly used molten $NaNO_3/KNO_3$ salts mixtures, *i.e.* up to 8 MJ/kg and ~ 0.5 MJ/kg, respectively [8,9]. Furthermore, due to the low energy density of molten salts mixtures, considerably large storage tanks are required to store adequate energy quantities [10,11]. In Table 1, different molten salts materials, like nitrates, chlorides and fluorides as well as metal hydride systems are listed according to their gravimetric and volumetric energy densities.

Magnesium hydride is considered as a suitable material for hydrogen storage applications, due to a hydrogen content of 7.6 wt.% [12] associated with hydrogenation/dehydrogenation reaction enthalpy of about 74 kJ/mol_{H2} [13–16], and to a high degree of reversibility (if doped with selected transition metal-based additives or in the presence of alloying elements) [17–24]. Already in 1990 Bogdanovic et al., [12] reported about the possibility to use MgH_2 as a reversible chemical energy storage system. Furthermore, direct steam generation inside the metal hydride reactor is technically possible [25].

As several authors stated, in order to maximize the profitableness of the heat storage system, the storage material must be cost efficient [9,10,17]. Facing this issue, in this work, the use of magnesium-based wastes is proposed as a potential cost-effective solution, as it is presented in Table 1. For Mg alloys, mainly processed as die-castings and alloyed with Al, no independent recycling pathway exists yet. Because of its light weight, Mg alloys are separated into the lightweight scrap fraction that is dominated by aluminum parts during the general scrap treatment. Since Mg is not of significant interest for recovery, a great part of end-of-life products made of Mg alloys ends up in landfills [26]. As Mg is nowadays considered as a critical raw material by the European Union, the development of an efficient recycling route is desirable [27]. The use of Mg swarf and wastes as raw material for the synthesis of metal hydride systems for energy storage applications can be one part of a Mg recycling concept [28].

In previous works of Pistidda et al., [38] and Hardian et al., [39], the use of waste magnesium alloys for hydrogen storage purposes was proposed. The utilized material in the work of Hardian et al. was stored in air for several weeks before it was milled together with 5 wt.% graphite in argon atmosphere [39]. Upon hydrogenation, MgH_2 forms and about 6 wt.% of H_2 can be stored into the material. At 350 °C and 13 bar_{H2} the Mg waste based system could store up to 90% of the overall hydrogen capacity in about 10 min. The dehydrogenation process was completed in about 10 min at 0.5 bar_{H2} and 350 °C. The system's stability was tested for over 70 hydrogenation/dehydrogenation cycles without any deterioration of material storage properties [39]. The work of Pistidda et al. reports the investigation of the hydrogen storage properties of two different Mg waste alloys, namely AZ91 and the Mg-10 wt.% Gd alloy [38]. The overall hydrogen storage capacity of the AZ91 material was measured at 6.25 wt.%, compared to a theoretical capacity of 6.9 wt.%. Furthermore, using high-energy reactive ball milling, the waste material was successfully employed as a starting reactant to synthesize magnesium amide. The hydrogenated waste was also used for substituting high purity MgH_2 in the $LiBH_4 + MgH_2$ reactive hydride composite system [38].

Based on these promising results for the low cost Mg waste material, a next step is taken in this work. Trying to understand the hydrogen storage properties of larger batches of MgH_2 obtained from waste alloys, Mg-Al waste powders were prepared and their properties investigated in an *in-house* built reactor. To describe the powder behavior, a specific simulation model that takes into account the materials rate limiting processes has been developed and validated for a broad range of experimental conditions.

2. Materials and methods

The as-received Mg-Al waste, taken as swarf and chips from the Hereon *in-house* workshop, was stored in air for

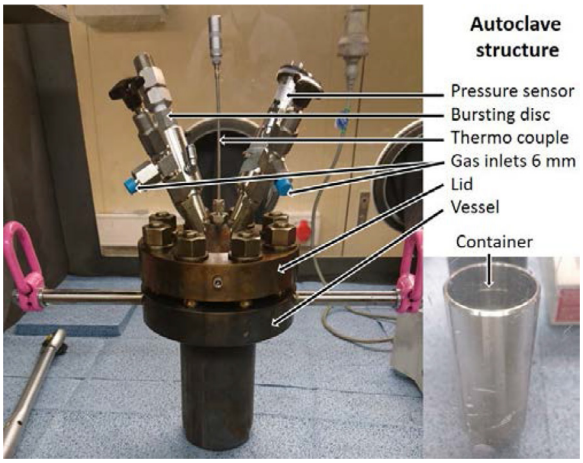

Fig. 1. Picture of the autoclave with installed setup (left) and inlet which contains the powder (right.

several months before starting this work. The material was milled in a *Simoloyer CM08* industrial mill from *ZOZ GmbH* for two hours under Argon atmosphere, with milling balls made of 100Cr6 chromium steel with a diameter of 5 mm and a ball to powder ratio of 1:20. Milling was perfomed in a cyclic process of 700 rpm/30 s and 300 rpm/30 s. After the milling treatment, the powder was kept under controlled atmosphere with oxygen and moisture concentration below 5 ppm. The milled powder was sieved for one hour in an *Analysette 3 Pro*-sieving machine (*Fritsch GmbH*) with a sieve mesh size of 63 μm. For the analysis of the hydrogen sorption kinetics an *in-house* built Sievert apparatus was used. For each measurement about 200 mg of material were utilized. To match the experimental conditions utilized by Hardian et al., the hydrogen absorption measurements were done at a pressure of 13 bar [39]. The chosen temperatures range between 260 °C and 360 °C. The hydrogen desorption measurements were carried out in the temperature range between 335 °C and 375 °C at 1 bar of hydrogen backpressure, after previous hydrogenation at 350 °C and 13 bar for 2 h.

For the experimental validation of the developed simulation model, a stainless steel reactor was used, shown in Fig. 1. The inner volume of the reactor is 250 ml. The reactor is thermally regulated by a heating jacket of 3 kW electrical power and equipped with a hydrogen mass flow controller with a measuring range between 2 and 100 std°l/min. The temperature is measured with a type K thermocouple inserted in the powder bed. For the experiments, a powder batch of 90 g was loaded into the reactor inlet. The quantity of hydrogen absorbed or released by the powder bed is determined by the use of the above mentioned mass flow meter. For the cycling experiments, the set hydrogen pressure and temperature conditions match those utilized in the Sievert apparatus. For the absorption measurements, the hydrogen supply was set to 13 bar at the pressure reducer, filling the line up to the volume flow controller. By starting the measurement, the valve of the volume flow controller is opened to 100%, to obtain the maximum hydrogen loading rate. For desorption conditions, the pressure in the reactor is held by the volume flow controller and opened to 100% at the beginning of the experiment. To have comparable starting conditions, after each desorption measurement, the reactor is kept for 10 min under dynamic vacuum (10^{-2} bar) to fully unload the powder bed.

To determine the material apparent activation energy for the hydrogen desorption process, a high pressure *DSC 204* from the company *NETZSCH* was utilized. Therefore, four temperature ramps of 1, 3, 5, and 10 K/min are used to desorb the material at 1 bar of hydrogen pressure.

The materials effective thermal conductivity was measured with a *TPS 1500* from *Hot Disc AB* under argon atmosphere using a kapton-insulated sensor of 6.4 mm diameter. The overall powder handling was performed in gloveboxes under a continuously purified argon atmosphere (O_2 and H_2O levels < 5 ppm). X-ray powder diffraction (XRD) was used to characterize the material composition. For this purpose a diffractometer *D8 Discover* from *Bruker* equipped with a Cu Kα radiation source ($\lambda = 1.5406$ Å) was utilized. SEM micrographs were acquired using a *Quanta SEM* from the company *ThermoFischer Scientific*.

The finite element method (FEM) simulation performed in this work was carried out using the software COMSOL Multiphysics® 5.5 and its physic modules heat transport in porous media, Brinkman-Equation and transport of diluted species.

3. Results and discussion

3.1. Reaction model

The role and influence of Al on the hydrogen storage properties of Mg have been discussed in several publications, in which a two-step reaction for the hydrogenation process of the $Mg_{17}Al_{12}$ phase is proposed [40–44].

$$Mg_{17}Al_{12} + 9\ H_2 \rightarrow 9\ MgH_2 + 4\ Mg_2Al_3$$

Upon hydrogenation, first $Mg_{17}Al_{12}$ forms Mg_2Al_3 and MgH_2, and then the freshly formed Mg_2Al_3 leads to the formation of additional MgH_2 and pure Al [40].

$$Mg_2Al_3 + 2\ H_2 \rightarrow 2\ MgH_2 + 3\ Al$$

Both reaction steps are fully reversible. In terms of thermodynamics, two plateaus can be seen in the PCI plot that correspond to the two reactions mentioned above. The equilibrium pressures for both reactions are higher than for the pure Mg/MgH_2 system, as the addition of Al was observed to destabilize the MgH_2 decomposition. This can be explained by the exothermic formation of Mg-Al compounds, while the desorption of MgH_2 is occurring [41,44]. The reaction enthalpy of the two step hydrogenation reaction that can be calculated for the first and the second plateau are -77.7 kJ/mol_{H2} and -62.7 kJ/mol_{H2}, respectively, which indicates only an observable enthalpy reduction in the second reaction step [41]. The inclusion of Al into the Mg/MgH2 system improves the hydrogenation/dehydrogenation rates as Al works as a heat transfer phase [44]. Due to the destabilizing effect of Al on

the MgH_2 phase and the elevated equilibrium pressure, faster desorption reaction kinetics appear for Mg-Al systems, having lower activation energies than for the pure Mg/MgH_2 system [40–42,44]. Some kinetic models describing the de-/hydrogenation reaction of Mg-Al-based systems are currently available, but none for MgH_2 systems containing only minor amounts of Mg/Al alloys and other alloying elements and impurities. As a result, novel reaction kinetic models for describing the de- and hydrogenation properties of Mg/Al-based waste materials for energy storage purposes are developed in this work.

In order to obtain a reaction model that can be applied and continuously adapts to the actual temperature and pressure conditions, the intrinsic rate-limiting step of the reaction must be identified. According to the slowest reaction step of the complete gas-solid reaction, different models can be chosen to describe the overall reaction kinetic. The selection of reaction models $f(\alpha)$, which are considered in this work, can be found in the supporting information (A). Four main sets of models are available, namely nucleation and growth models, geometrical contracting models, diffusion models and autocatalytic models (which are not considered in this work) [45]. The best fit indicates the rate-limiting step of the reaction and can be used to further derivate the thermodynamic dependencies. The integral of the reaction rate function $F(\alpha)$ is used to obtain an equation that can be directly used, to fit the experimental data set, which is recorded as the consecutive sum of absorbed hydrogen. Therefore, the equation for the reaction rate $d\alpha/dt$ (α = reacted fraction and t = time) is rearranged to:

$$\frac{d\alpha}{dt} = k\ (T, p)\ f(\alpha)$$

$$\frac{d\alpha}{f(\alpha)} = k(T, p)\ dt$$

$$F(\alpha) = \int \frac{d\alpha}{f(\alpha)} = k(T, p)\ t$$

The reduced time method, by Jones et al. and Sharp et al., [46,47] is used in this instance, as it gives more precise indications for the goodness of fit than standard fitting functions. By having 3 quality parameters, namely the slope, the intercept and the coefficient of determination of the fitted curve, the model can be chosen according to the number of parameters that are the closest to the ideal fit. The applied approach can be found in the work of Julián Atilio Puszkiel [45]. After obtaining the reaction kinetic constant k, the activation energy E_a and the frequency factor A are determined by using the Arrhenius function.

$$k(T, p) = A \exp\left(\frac{-E_a}{RT}\right) f(p)$$

Different pressure dependency functions are available in literature for the Mg/MgH_2 system [48,49] as well as for the Mg-Al alloy system [41]. Due to the unsatisfactory results obtained by the use of the activation energy values reported in literature, new pressure dependency functions are derived in this work [48,50–55].

3.1.1. Absorption

The maximum achieved hydrogen storage capacity during the absorption measurements was 5.8 wt.%. To model the reaction kinetics, only the dimensionless fraction of the reaction product α is used. The attempt to fit the overall reacted fraction with the reaction models proposed in literature [45,47,56] (see supplementary data (A)), led to unsatisfactory results. Therefore, a new approach is proposed and implemented here. The reaction is subdivided into two regions. The first region includes the reaction fractions between 10% and 50%, whereas the second region includes the reaction fractions between 50% and 90%. The fitting results obtained for the different reaction regions for all temperature ranges are summarized in the supporting data (B). Obviously, that for the investigated range of temperatures, the rate limiting steps of the two regions are different. In the first region, the fitting results indicate that the rate limiting step is the nucleation and growth mechanism following the one-dimensional Johnson-Mehl-Avrami (JMA 1) model. For the second region, the fitting results indicate that the rate limiting step changes to a diffusion controlled process. Table 2 gives an overview of the kinetic constants and of the best fitting models, depending on the temperature. Independently from the applied temperature, the first reaction region fits the JMA 1 model the best. Instead, for the temperatures 280 °C, 300 °C, 320 °C, and 340 °C the second reaction region fits the best the diffusion controlled (D 3) model, whereas for the temperature 360 °C the D 4 model fits better. The D 4 model is an improvement of the D 3 model obtained by additionally taking into account the Fick's law for radial diffusion for solid spheres with increasing product layer [57]. However, since the D 3 model of Jander [58] fits best for a greater part of the absorption reactions, it is selected for the modeling of the second reaction region for all reactions studied here for direct comparison.

These results show that the rate limiting process changes as the reaction proceeds. This finding can be explained by the fact that in the initial state, the material consists mainly of pure Mg and some $Mg_{17}Al_{12}$ particles (as shown in the XRD pattern in the supporting information (C)), in whose crystal lattices hydrogen can diffuse easily. However, after a hydride layer is formed at the topmost surface of the particles, further hydrogen diffusion is constrained. This behavior is well known for Mg-based materials, and can explain the change of the reaction model observed in the two reaction regions [59–62].

To determine the parameters for the Arrhenius term, it is important to exclude the pressure dependency function. Therefore, different pressure functions from literature are used. For each function, the activation energy is calculated and interpreted. Hence, the model equation is rearranged as follows:

$$k(T, p) = A \exp\left(\frac{-E_a}{RT}\right)\ f(p)$$

$$\ln\left(\frac{k}{f(p)}\right) = \ln A - \frac{E_a}{RT}$$

Table 2
Best fitting reaction models regarding the temperature for absorption, the reaction regime and reaction rate constants.

Temperature [°C]	$0.1 \leq \alpha \leq 0.5$		$0.5 < \alpha \leq 0.9$	
	Reaction model	Kinetic constant k [1/s]	Reaction model	Kinetic constant k resulting for the D 3 reaction model [1/s]
260	JMA 1	1.09E-3	D 3	8.79E-5
280	JMA 1	1.97E-3	D 3	1.29E-4
300	JMA 1	3.45E-3	D 3	1.88E-4
320	JMA 1	5.17E-3	D 3	2.83E-4
340	JMA 1	5.51E-3	D 3	3.37E-4
360	JMA 1	3.04E-3	D 4	2.90E-4

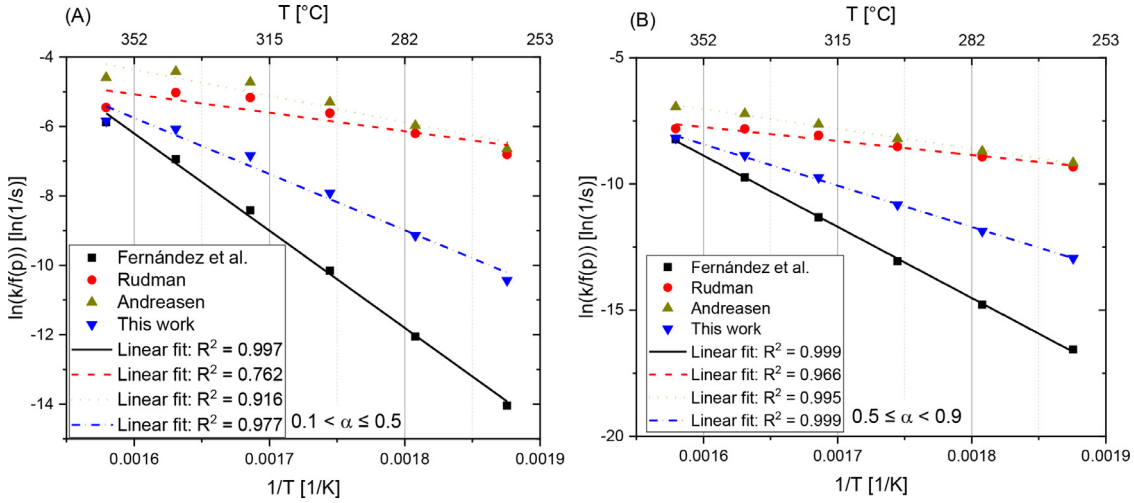

Fig. 2. Determination of absorption activation energy and frequency factor with isobaric kinetic measurements for different pressure functions and reaction regimes. (A) First region and (B) second region.

Table 3
Absorption activation energies and frequency factors according to the used pressure functions from literature and by derivation in this work.

Source	Proposed pressure function	$0.1 \leq \alpha \leq 0.5$		$0.5 < \alpha \leq 0.9$	
		Activation energy E_a [kJ/mol$_{H2}$]	Frequency factor A [1/s]	Activation energy E_a [kJ/mol$_{H2}$]	Frequency factor A [1/s]
Fernández and Sánchez [48]	$f(p) = (\frac{p}{p_{eq}} - 1)^2$	232.9	5.80E16	234.7	5.82E15
Rudman [49]	$f(p) = (1 - \frac{p_{eq}}{p})^{\frac{1}{2}}$	44.2	3.09E1	46.0	3.00E0
Andreasen [41]	$f(p) = 1 - (\frac{p_{eq}}{p})^{\frac{1}{2}}$	63.1	2.37E3	64.8	2.30E2
This work	$f(p) = \frac{p}{p_{eq}} - 1$	134.4	5.36E8	136.2	5.38E7

The equilibrium pressures at the measured temperatures are taken from the pure Mg/MgH$_2$ system obtained by Oelerich et al. [61] The results of the linear fitting are shown in Fig. 2 and the used pressure functions in Table 3 for the first and second reaction regions. The values obtained for the activation energies lie far apart for each pressure function, whereas the differences among the two separate reaction regions, are small.

Typical values for the activation energy of pure Mg systems are according to literature in the range between 90 and 140 kJ/mol$_{H2}$ for the absorption [48,50–52,60]. Since the resulting activations energies are outside this range, the pressure functions from literature obtained for pure Mg [48,49] as well as for Mg/Al alloys [41] are considered not suitable to model the reaction kinetics of recycled Mg/Al based waste from this work. Hence, the pressure function $f(p) = p/p_{eq} - 1$ is proposed, since it gives a reasonable activation energy comparing to the pure Mg system and leads to a good fitting of the kinetic curves.

3.1.2. Desorption

In contrast to the absorption reaction, the fitting results obtained for the desorption kinetics indicate that the overall reaction process can be described using just a single model. Thus, the model fitting is applied for the full range between 10% and 90% of the reaction. The reaction model that fits best is the CV 2 model, meaning a geometrical description of the reaction rate by a contracting area of a cylinder towards the cen-

Table 4
Best fitting reaction models regarding the temperature for desorption and the reaction rate constants.

Temperature [°C]	Reaction model	Kinetic constant k resulting for the CV 2 model [1/s]
335	JMA 2	5.90E-4
345	CV 2	9.88E-4
355	CV 2	1.48E-3
365	CV 2	2.15E-3
375	CV 2	3.03E-3

Table 5
Desorption activation energies und frequency factors according to the used pressure functions from literature and by derivation of this work.

Source	Proposed pressure function	Activation energy E_a [kJ/mol$_{H2}$]	Frequency factor A [1/s]
Fernández and Sánchez [48]	$f(p) = 1 - (\frac{p}{p_{eq}})^{\frac{1}{2}}$	91.4	8.93E4
Fernández and Sánchez [48]	$f(p) = 1 - \frac{p}{p_{eq}}$	78.0	1.09E4
Rudman [49]	$f(p) = p_{eq}^{\frac{1}{2}} - p^{\frac{1}{2}}$	41.7	6.57E7
This work	$f(p) = \frac{p_{eq}-p}{p_{eq}^2}$	164.0	2.92E11

ter at constant interphase velocity [45,56]. The decomposition kinetic of the MgH_2 system has been accurately described by Stander [60]. In this work, a change of the reaction-limiting step for various temperatures is identified. For high temperatures, a constant Mg-MgH_2 interface velocity model describes the rate-limiting step. The bi-dimensionality of the process is explained by the change from the tetragonal structure of the hydride to the hexagonal close-packed structure of the Mg metal. This leads to a cylindrical shape of the MgH_2-Mg interface. As the hydride core decomposes, the H atoms diffuse through the metal lattice and recombine to the gas at the particle surface, so that no diffusion through hydride phases limits the reaction. For the $Mg_{17}Al_{12}$ system, similar results are present in literature, describing the decomposition as a bi-dimensional interphase transformation process [41].

Table 4 provides an overview of the best fitting reaction models for the desorption and the resulting reaction rate constants at different temperatures. The desorption curves are best described by the CV 2 model, although for the desorption reaction at 335 °C, the JMA 2 model provides slightly better fitting parameters. This could result from the proximity to the equilibrium condition, so that the low temperature limits the reaction to start. For this reason, the nucleation and growth phenomena start limiting the reaction. The same was also observed by Stander, who reported the change of the limiting process with increasing temperature [60]. Similarly to the absorption process, the Arrhenius plot resulting from the reaction rate constants and estimated pressure dependency determines the activation energy for the desorption process, as shown in Fig. 3.

The pressure functions taken from literature and proposed in this work are listed in Table 5. Taking the pressure functions from literature, values for the activation energy between 41.7 and 91.4 kJ/mol$_{H2}$ are obtained, which seem too low for the dehydrogenation of a Mg-based system. For this reason, in contrast to the absorption reaction modeling, the activation energy for the desorption process was determined based on DSC measurements using the Kissinger method (see supplementary data (D)). As it can be seen from Fig. 31, the DSC

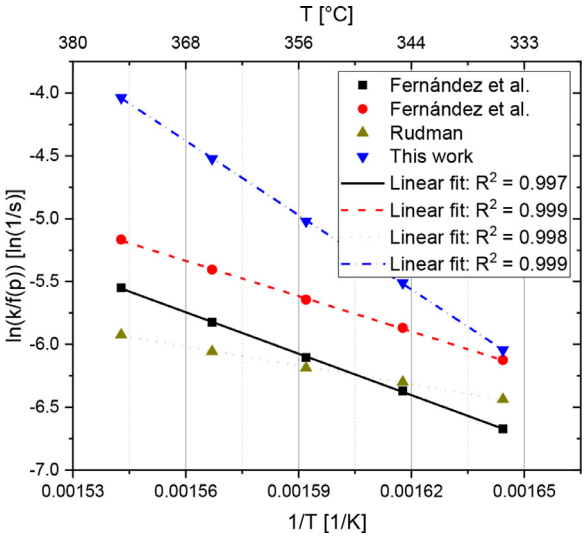

Fig. 3. Determination of desorption activation energy and frequency factor with isobaric kinetic measurements for different pressure function.

traces recorded at 1, 3 and 5 K/min appear to be constituted of two overlapping signals. Whereas, for the measurement acquired with a heating ramp of 10 K/min a single endothermic signal is observed. The reason for the presence of two overlapping signals at low heating rates is most likely due to inhomogeneity in the material particle size distribution (as visible in Fig. 32 in the supplementary data (D)) that leads to the dehydrogenation of the bigger MgH_2 particles at higher temperatures. We expect that this phenomenon is not visible for the measurement carried out at 10 k/min because of the coalescence of the two signals while shifting to higher temperatures. The occurrence of agglomeration and coarsening events during material cycling at high temperatures can explain the presence of particles of significantly varied sizes. From the DSC results, an activation energy of 168.7 kJ/mol$_{H2}$ is obtained from the Kissinger plot using the peak temperatures. Comparing the activation energies resulting from the fitting of the kinetic measurements with the value from the

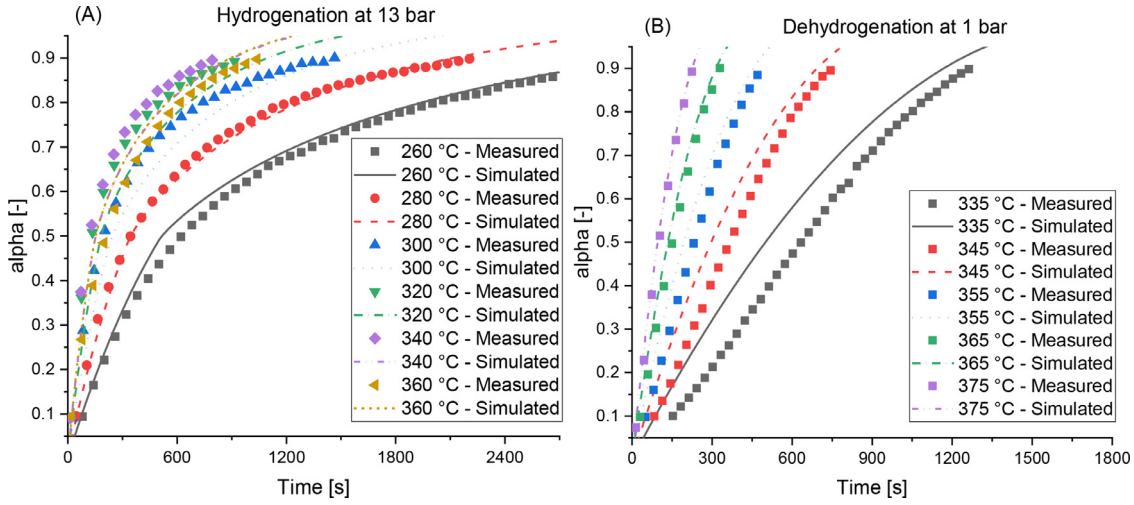

Fig. 4. Measured and simulated hydrogen (A) absorption and (B) desorption reaction kinetic.

Kissinger method, a high discrepancy is observable. Therefore, the pressure functions from literature are not considered for the desorption reaction model and a new function of $f(p) = \frac{p_{eq}-p}{p_{eq}^2}$ is implemented, to achieve a more precise activation energy. As the result, the obtained activation energy value (listed in Table 5) is in a better agreement with the results obtained via DSC. Additionally, the typical values for the activation energy of desorption in the Mg/MgH_2 system are in the range of 120 – 170 kJ/mol_{H2}, which confirm the validity of the new pressure function [51,53–55,63]. According to Li et al., adding 10% Al to the Mg/Mg_{H2} system reduces the activation energy from 173 kJ/mol_{H2} in the pure system to 164 and 158 kJ/mol_{H2} in the 20 h ball milling and as-casted systems, respectively [40]. The literature values fit together quite well when compared to the value obtained for the Mg/Al based waste material studied in this work.

In Fig. 4, the measured kinetic curves (represented by symbols) for absorption and desorption processes are plotted together with the simulated reaction kinetic (represented by lines) obtained from the developed reaction model. For the absorption reaction, the change of the reaction model at the 50% of the reacted fraction is clearly visible from the discontinuity in the slope. In general, the simulated curves fit the experimental data well, although for high temperatures a small mismatch for the second reaction regime occurs. For the desorption reaction, a good match between experimental and simulated data is observed. For lower temperature, the simulation predicts a faster reaction rate than the measured one. A reason for this inconsistency could be found in the small reaction driving force under conditions close to the equilibrium.

To obtain a reaction model that unambiguously describes the kinetic pressure dependencies, a large number of measurements in a broad range of temperature and pressure conditions should be taken into account. In this work, even though a limited number of kinetic data is available, a model that adequately describes the reaction kinetic for recycled Mg is developed.

3.2. Simulation model

For simulating the heat distribution as well as the hydrogen uptake and discharge during the bulk reaction via FEM, a 2D axisymmetric model of the reactor geometry is chosen. By rotating the 2D axisymmetric model for 360 ° around the symmetry axis, a 3D model is generated, whose slices are behaving equal for all angles. The governing heat transport equation for general balances of a specific domain regarding a volume element given now in W/m^3 can be written as:

$$(\rho c_p)_{eff} \frac{\partial T}{\partial t} = \sum_{i=1}^{n} \dot{q}_{convective,i} + \sum_{j=1}^{m} \dot{q}_{transfer,j} + \sum_{k=1}^{p} \dot{q}_{source/sink}$$

The change of temperature inside a domain is dependent on the sum of the n convective heat fluxes, which go into or out of the domain by mass transportation, the sum of the m heat transitions by conduction or transfer and the sum of the p heat sources or sinks, with n, m and p as integers. For each domain of the simulation geometry, different terms can be neglected, as for solid parts like the body of the autoclave no heat sources or convective heat transportation occurs. However, for the domain of the storage material (*i.e.* Mg-Al waste), all terms are considered. The heat sources and/or sinks are given by the reaction enthalpy and the reaction rate for the absorption or desorption processes.

$$\dot{q}_{source/sink} = r \ \Delta H_{absorption/desorption}$$

In the following section, the reaction kinetics are modeled and derived with respect to the material transformed fraction. To obtain the quantitative amount of absorbed hydrogen per volume unit, the maximum possible capacity x_{max} in wt.% is considered and multiplied by the bulk density ρ_{bulk} of the Mg-Al waste [64].

$$r = \frac{d\alpha}{dt} \ x_{max} \ \rho_{bulk}$$

The convective heat transport can be described by:

$$\dot{q}_{convective} = \left(\rho_{H_2} c_{p,H_2}\right) \vec{u}_{H_2} \ \nabla T$$

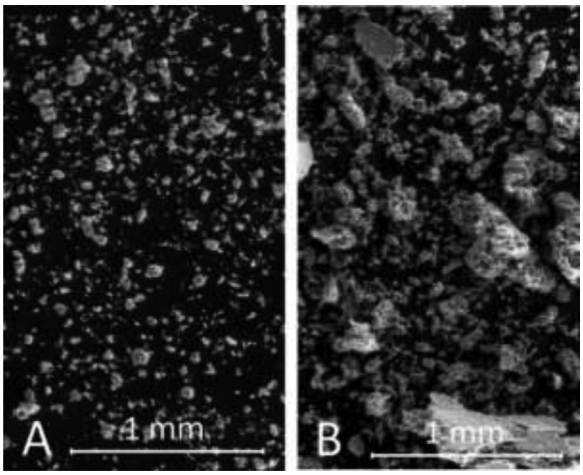

Fig. 5. SEM micrographs of cycled Mg-Al waste from A) loose top part and B) sintered fraction in the lower part of the autoclave.

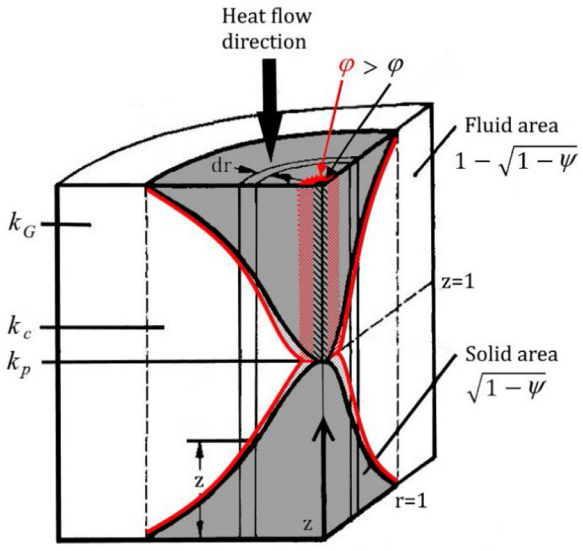

Fig. 6. Unit cell according to Zehner with increased particle contact area regarding the flattening coefficient [66,67].

Due to the low density of hydrogen, the convective heat transported into or out of the system has a low impact on the overall balance [65]. More crucial is the heat transport by conduction through the powder bed, which is given by:

$$\dot{q}_{transfer} = k_{eff}\ \nabla T$$

The effective thermal conductivity k_{eff} is assumed homogeneous over the powder bed, with a combination of gas and solid heat conduction. In this simulation model approach, the semi-empirical model of Zehner and Schlünder [66–68] is used and modified to match certain properties of the metal hydride bed at higher temperatures. The model describes a cylindrical unit cell, in which two solid particles are in contact surrounded by a gaseous phase, as shown in Fig. 6. The heat conduction is separated into two regions: The thermal conduction through the inner core of the cell, in which non-continuous gas conduction k_c and solid-solid conduction through the contact area k_p appears and the continuous gas conduction k_G surrounding the inner core. A radiation term k_{rad} is also considered within the gas phase.

$$k_{eff} = \frac{k_{bed}}{k_f}$$

$$k_{bed} = \left(1-\sqrt{1-\psi}\right)\ \psi\ \left[\left(\psi - 1 + k_G^{-1}\right)^{-1} + k_{rad}\right] + \sqrt{1-\psi}\ \left[\varphi k_p + (1-\varphi)k_c\right]$$

The decisive factor for this subdivision is the porosity ψ, which can also be used to describe the geometric conditions in the unit cell. In the Zehner model, the fraction of solid conduction in the inner core is given by the flattening coefficient ϕ. Since the powder bed gets sintered in the high temperature bottom region of the reactor (see Fig. 33, in the supplementary data (E)), the contact areas between the particles lower their thermal resistance. In Fig. 5, SEM micrographs of the cycled material from different regions of the reactor are shown. The small particles in the loose powder are shown on the left (A), whereas on the right hand side, the growth of the agglomerates, due to sintering, becomes obvious (B). These bigger chunks were scraped off of the bottom part of the sintered material specimen (In Fig. 33 SI a picture of the complete sintered material for the whole cross section is shown.).

During the sintering process in the high temperature region in the reactor, a solid connection grows between the particles surfaces, leading to a higher portion of thermal conduction through the solid phase. By measuring the effective thermal conductivity after the cycling, the flattening coefficient is adapted to fit the modeled values to the measured ones. In Fig. 6, the adapted flattening coefficient is illustrated in the frame of the unit cell of Zehner's model, adapted from [66,67]. The red full-tone color at the upper projected area marks the projected increased junction of the sintered particles. The measured effective thermal conductivity value (measured in an argon atmosphere and at room temperature) of the sintered Mg-Al waste powder is 1.5 W/(mK), whereas for a bed of loose powder this value would be only 0.2 W/(mK). The flattening coefficient is found to be 0.036 and 0.004, respectively. Typical values for loose and fine granular materials lie between 0.001 for broken particles and 0.025 for round spheres. Variables like pressure, temperature or particle size are considered in this model.

During hydrogen absorption, a material volume expansion of 30% is considered, that, in turn, leads to a dynamic decrease in porosity [69,70]. The complete set of equations for the determination of k_{eff} can be found in Ref [68] together with the derivation from [66,67].

For the complete heat balance of the simulation, the external heat source of the reactor is required for domains with external boundaries. Therefore, a PID controller of the heating jacket was also implemented in the software with the parameters $k_P = 10\ W/°C$, $k_I = 0.001\ W/(s\,°C)$ and $k_D = 0\ (Ws)/°C$. The maximum power output is limited to 3 kW. At the

surface of the autoclave, which is not covered with the heating jacket, the boundary condition is set to a natural convection surrounding with a heat transfer coefficient of 1 W/(m^2 K) to a room temperature of 20 °C.

Between the Mg-Al waste particles and the wall of the container, the thermal conduction is limited, due to a higher porosity and low solid-solid contact areas at the wall of the reactor inlet. Commonly, a thermal contact resistance can be defined at this boundary. In literature, a broad range for thermal contact resistances or rather heat transfer coefficients from the wall to the powder can be found from 30 to 2500 W/(m^2 K) [71–73]. These values are strongly dependent on the porosity, absorption state, gas pressure and general material properties. Within this work, the thermal contact resistance is set to 1000 W/(m^2 K), which allow achieving a good agreement between the simulated and the experimental data, by performing a parametric sweep. Besides the direct powder-wall interface, also a solid-gas-solid interface area must be considered between the powder container and the reactor wall. This boundary is modeled as a thin layer of gaseous hydrogen in a 100 µm thick gap with the gas properties implemented in the COMSOL Multiphysics® database. An overview of the domains and the boundary conditions as well as the used material properties, variables and equations for the simulation can be found in the supplementary data (F, G and H). The temperature dependent material properties for the different steels, like specific heat capacity or thermal conductivity, of the autoclave are taken from the work of Richter [74]. In contrast to the experimental reactor design, for the simulation model the hydrogen inlet is shifted to the center for simplicity reasons (which does not matter here, because a 2D axisymmetric model is used). In addition, the reactor pressure sensor and bursting disk are not implemented in detail, only the connecting pieces are considered in this model design. Regarding the simulation starting conditions, a timeframe of 5 h is simulated to get a constant temperature distribution field within the system, in which the PID controller reaches a stable output value. For the mass transport the Brinkmann equations are used, as they are implemented in COMSOL Multiphysics®, considering free gaseous flow and flow in porous media including the permeability of the powder bed. The permeability is calculated with the Carman-Kozeny equation, depending on the particle sizes and the porosity [75].

3.3. Scaled-up system results

3.3.1. Absorption experimental results

For all the performed absorption experiments, the hydrogen flow is given on left side of Fig. 8(A) for the first two minutes and Fig. 9(A) for the following 30 min. The temperature profiles for each absorption experiment are plotted in Fig. 7 (A – dotted lines). The temperature of the powder beds rises within about two minutes to their maxima and then decreases with different rates, depending on the initially applied temperature.

The rise of the powder bed temperatures for the experiments performed at an initial temperature of 260 °C, 280 °C, 300 °C and 320 °C leads to peak temperatures of 348 °C, 362 °C, 373 °C and 375 °C respectively. This phenomenon is the consequence of the large amount of heat released during hydrogen absorption. The peak temperature values are naturally below the equilibrium temperature at the applied hydrogen pressure (386 °C at 13 bar), as the hydrogenation process is thermodynamically self-regulating in the two-phase region [76]. The temperature governs the reaction kinetics, as observable in Fig. 8, which displays the increasing hydrogen flowrate for the experiments at initially low temperatures. The flowrate accelerates for one minute for the absorption starting at 260 °C and for 30 s for the one starting at 280 °C. Due to the heat up of the powder bed, more favorable temperatures for the reaction kinetic are reached, leading to the accelerating absorption reaction. For the experiments at 300 °C the increasing flowrate last about 15 s and for the starting temperature at 320 °C only a few seconds of rising flowrate

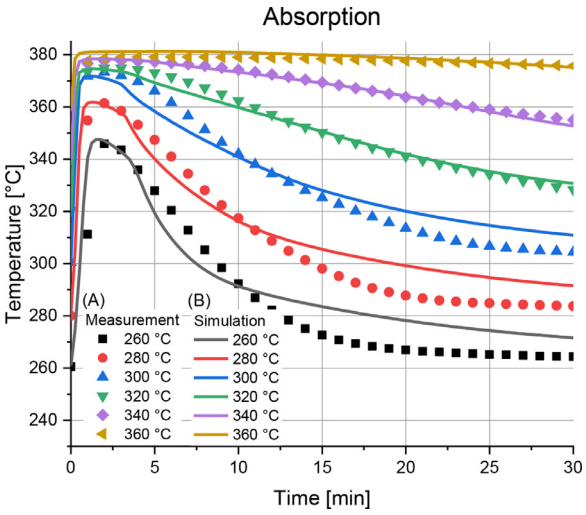

Fig. 7. Absorption measurements with the autoclave: Temperature development inside the powder bed for (A – dotted lines) the experiments and (B – solid lines) the simulations.

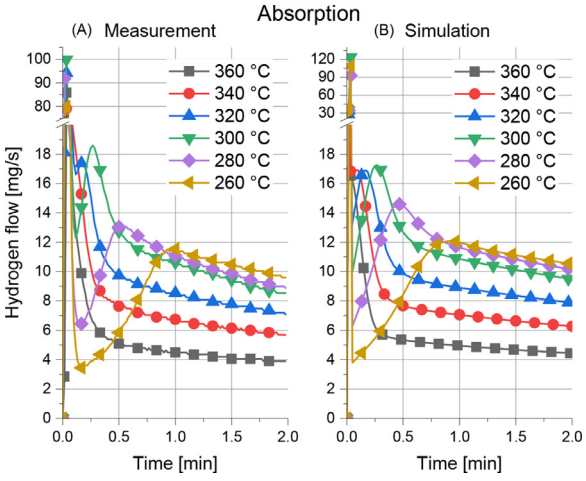

Fig. 8. Absorption measurements with the autoclave: Initial hydrogen flow into the autoclave for different initial temperatures for (A) the experiments and (B) the simulations in the first 2 min.

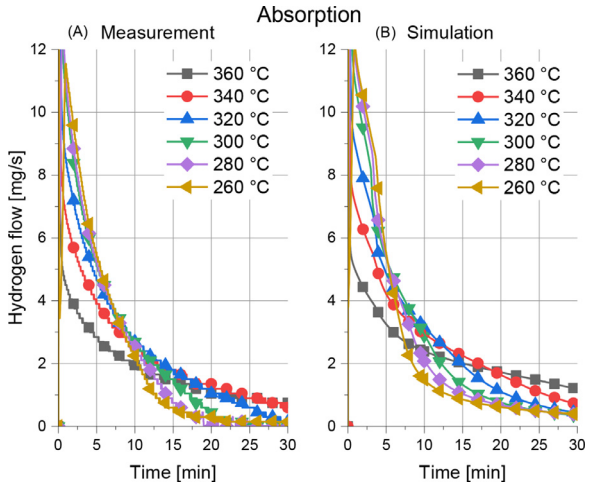

Fig. 9. Absorption measurements with the autoclave: Hydrogen flow into the autoclave for different initial temperatures for (A) the experiments and (B) the simulations until 30 min.

are identified. The reason for this is the smaller temperature difference between the starting temperature and the equilibrium temperature. However, for the measurements performed at powder bed starting values higher than 320 °C, the hydrogen flowrate continuously drops, caused by an overall sensible decrement of the hydrogenation kinetics. This is due to the increases of the beds temperature to values that are close the equilibrium temperature.

Indeed, for the experiments at 340 °C and 360 °C starting temperatures, the peak temperatures reached inside the powder beds are 378 °C and 379 °C, respectively. After 30 s the hydrogen flow of the 360 °C experiment becomes the lowest compared to the other starting temperatures whereas after 60 s the flowrate of the 260 °C experiment becomes the fastest. It changes over time, which is indicated in Fig. 9, that the flowrate of the highest initial temperature 360 °C becomes the fastest again after 27 min and the flowrate of the lowest initial temperature gets the slowest after 11 min. By achieving the favorable kinetic temperature with the own heat generation of the reaction, the fast absorption is only maintained as long as the heat is sufficient to keep this temperature. This is valid for lower initial powder bed temperatures, whereas at high initial temperatures, the resulting heat prevents an ideal temperature level.

Since the heat of reaction is not actively dissipated, the temperature remains at high values, prolonging the overall reaction time. As an example, for the experiment performed at an initial powder bed temperature of 360 °C, after 30 min from the starting of the experiment, the temperature is still above 370 °C as shown in Fig. 7 (A – dotted lines). Since the heating jacket has a set point of 360 °C, in this case the temperature difference between the powder bed and the wall of the reactor remains small, thus reducing the heat transport out of the system. For this reason, due to the reduction of the overall reaction rate, the hydrogen flowrate into the reactor (Fig. 9(A)) decreases the fastest in the case of the experiment performed at an initial powder bed temperature of 360 °C.

3.3.2. Absorption simulation results

In Fig. 7 the temperature profiles from the experiments (A – dotted lines) are compared to the results from the simulation model (B – solid lines). The comparison between the measured and the simulated temperature trends shows a good agreement between the two sets of data. However, in the experimental data, the powder bed temperatures, after reaching the peak temperatures, seem to decrease back to the starting value faster than in the simulated measurements. This tendency is better recognizable for the measurements performed at a lower starting temperatures of the powder bed. In fact, for the measurements performed at initial temperature values between 260 °C and 300 °C, the powder bed reaches a stable temperature level within 30 min from the starting of the process, whereas in the simulated data longer time intervals are needed for reaching a stable temperature value. In addition, the measured and simulated hydrogen flow are in good agreement, as shown in Figs. 8 and 9. For the measurements performed at different starting temperatures, a clear trend of the initial hydrogen flowrate is clearly visible. In fact, this value increases faster in the first minute when decreasing the initial temperature. Although the simulated data resembles the one of the experiments, it is possible to notice that the hydrogen flow for lower temperatures is decreasing faster than in the experimental data, Fig. 9. The measured hydrogen flow at the 260 °C after 10 min absorption is 2.25 mg/s, whereas the simulated data show a flow of 1.47 mg/s. In contrast, after 25 min, a small hydrogen flow of 0.48 mg/s is still indicated in the simulated data whereas no hydrogen flow is detected after the same time in the experimental data. The small differences, observed in the simulated hydrogen flow of Figs. 8 and 9, lead to obtaining small discrepancies between the simulated and the experimentally measured temperatures of the powder bed (Fig. 7). In fact, in the simulated data, the temperature values remain 10 to 20 °C higher after 25 min from the starting of the experiment. For absorptions at temperatures higher than 300 °C, the results of simulation and experiment are in perfect agreement.

3.3.3. Desorption experimental results

In Fig. 10 (A – dotted lines) and Fig. 11(A), the powder bed temperatures and the hydrogen flowrates are shown for the desorption processes at different starting temperatures. During these processes, depending on the initial starting temperature values, different minimum peak temperatures are reached, as displayed in Fig. 10 (A – dotted lines).

It must be mentioned that, in contrast to the absorption measurements, during the desorption measurements the hydrogen pressure, inside the reactor, is maintained constant at quasi-ambient conditions. Since the reactor is connected with the gas release line to the outside of the laboratory, a certain pressure drop in the piping must be overcome. This pressure drop is proportional to the volumetric flow through the pipe. The general definition to the pressure drop is given as [68]:

$$\Delta p = \zeta \ a \ \frac{\rho \ u^2}{2}$$

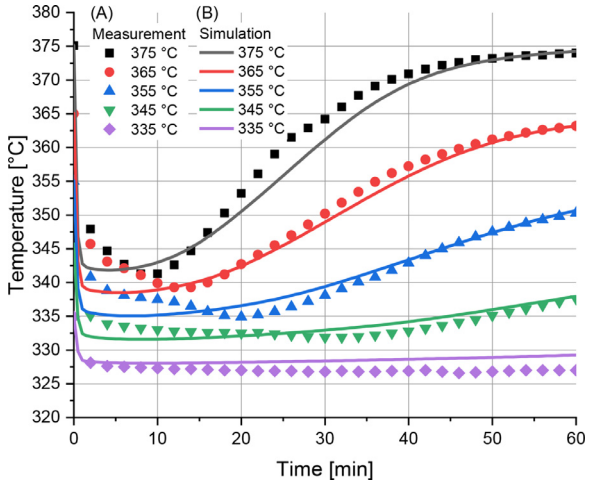

Fig. 10. Desorption measurements with the autoclave: Temperature development inside the powder bed for (A – dotted lines) the experiments and (B – solid lines) the simulations.

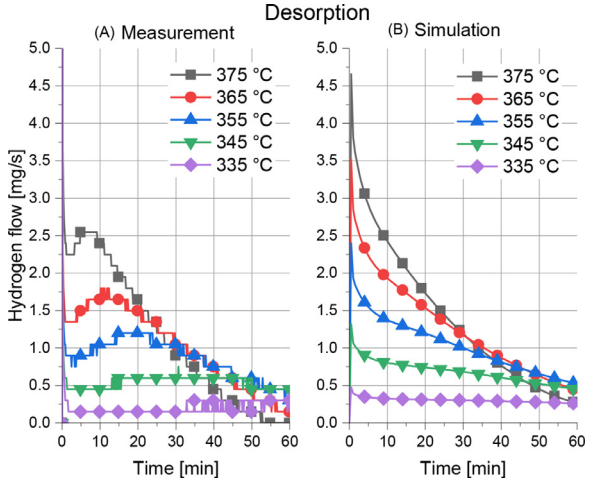

Fig. 11. Desorption measurements with the autoclave: Hydrogen flow out of the autoclave for different initial temperatures for (A) the experiments and (B) the simulations.

The factor a gives the type of the flow phenomenon and ζ the drag coefficient. With rising velocity of the flow, a higher pressure gradient must be provided as a driving force. At higher starting powder bed temperature, the material begins to release hydrogen with higher initial flow, see Fig. 11(A). For this reason, the pressure that sets itself in the autoclave is higher than the experiments with lower initial temperature. As a result, this might causes the minimum peak temperature values to differ within the desorption measurement series. The desorption pressure of the system varies from 1.5 to 2.4 bar at 325 to 345 °C, respectively [61]. Delhomme et al., [77] already discussed the great influence on the equilibrium temperature of small pressure variations at low system pressures for the MgH_2 system, especially in the desorption process. The measured pressure development can be found in the supplementary data (I).

Moreover, the temperature profiles of the measurements display a prior shoulder before the minimum peak is reached,

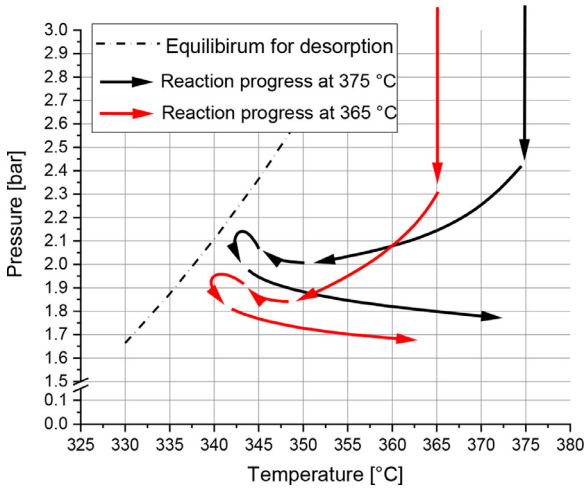

Fig. 12. Schematic reaction progress following the desorption measurements with the autoclave at 375 and 365 °C initial temperature in a pressure-temperature diagram.

see Fig. 10 (A – dotted lines). By comparing the hydrogen flow (Fig. 11) with the temperature development, their relevant points (maximum flow and minimum temperature) are synchronous for each experiment. After the first drop of the flow, coming from the gaseous phase, the hydrogen flowrate increases in the first minutes as the reaction is accelerating, see Fig. 11(A). For the measurements at 375 °C, 365 °C 355 °C and 345 °C the maximum flowrate is reached after 8, 11, 19 and 31 mins, respectively. During the acceleration of the hydrogen flow, an increasing pressure drop has to be overcome, therefore the pressure inside the system rises consequently. For this reason the reaction rate is hindered, retarding the temperature drop. This reflects in the shoulder noticeable before the actual peak. This behavior is illustrated in Fig. 12. The lower the initial temperature of the experiment is, the more pronounced is the shoulder that precede the peak temperature. The 335 °C desorption measurement shows no shoulder before the peak temperature. The motivation for this is found in the low initial temperature, which starts already close to the thermodynamic equilibrium. Because of this, the driving force is too small to accelerate the reaction and to build up enough pressure to observe the same behavior seen in the other measurements. Nevertheless, it is possible to claim that the higher the initial powder bed temperature, the faster the overall desorption reaction occurs.

Although the intrinsic kinetic of the desorption is faster than the one of the absorption, the scaled-up system needs longer times for the hydrogen release than for the loading. The fast pressure drop leads to a sudden decrease of the effective thermal conductivity inside the hydride bed, which limits the heat transportation into the system. The heat, coming from the autoclave wall, only slowly recovers the temperature of the bed. Moreover, the heating jacket, which determines the amount of heat going into the system, is controlled by the temperature of the reactor wall. This last value does not change at all, so that no surplus heat is provided, which would be needed for the desorption reaction. If the controller

measures the decrease in the wall temperature, more heat is applied to the system.

3.3.4. Desorption simulation results

By comparing the experimental and simulated data, it becomes obvious that the discussed phenomena are not reproduced with the same accuracy as for the absorption reaction. For the temperature profiles, a good agreement to the peak temperatures and the overall slope of the temperature is achieved (Fig. 10 (B – solid lines)). Although the interaction between the hydrogen flowrate, the pressure drop and the pressure level in the vessel is not implemented in the simulation, the peak temperatures could be precisely predicted by setting the measured pressure from the experiment as desorption pressure in the simulation. Focusing on the minimum peak shape, the measurements show a prior shoulder, which does not appear in the simulation results. The reason for the mismatches lies in the fixed value of the desorption pressure in the simulation. Although the values are taken from the experiments, no dynamic increase or decrease is allowed. For this reason, a dynamic change for the pressure is not possible, no matter if the desorption reaction accelerates and the pressure drop of the piping system rises caused by the increased hydrogen flow. The simulated conditions represent the ideal case, in which every released hydrogen molecule directly leaves the system. That is why, the initial temperature drop is reaching the lowest possible temperature directly with no delay. Looking at the hydrogen flow in Fig. 11, the simulation data do not show an initial limitation in the flow, as indicated by the experiments. The slope of the flowrate is continuously decreasing instead. This missing limitation could be explained by the absence of the pressure increase during the first minutes, which leads to a smaller dehydrogenation driving force. Another reason could be the setting of the PID controller in the simulation. In the experiments, an inertia between the temperature decrease and the response of the heater is recognized. Since the controller settings of the heating jacket were self-optimized and not accessible, the settings for the simulation were identified during the setup of stationary heat up simulations. For this reason, the controller could have undetected finer control characteristic. For small temperature drops the controller could directly react and heat up the system faster. Even with these hindrances, in general, the magnitude of the flows and the trend for the different desorption experiments are in good agreement.

4. Conclusions

Mg/Al-based waste combined with hydrogen is a potential candidate for thermal energy storage, since the waste material is cost neutral, can be stored in air until it is milled to fine powder and has very good thermodynamic and kinetic properties for the hydrogenation and dehydrogenation reaction. By absorbing 5.8 wt.% hydrogen, the storable amount of energy, regarding the reaction enthalpy of the Mg/MgH_2 system, is more than 2.1 MJ/kg of Mg waste. Kinetic measurements are done under absorbing pressures of 13 bar and desorbing pressures of 1 bar at temperatures between 260 °C and 375 °C. By taking thermodynamic data from the pure MgH_2 system, the kinetic models for ab- and desorption are derived. In the absorption reaction, a shift of the rate limiting process along the reaction process is identified and modeled accordingly. Consequently, new pressure functions for the Mg/Al based waste system are implemented in this study and activation energies of 134 – 136 kJ/mol_{H2} for the absorption and 164 – 169 kJ/mol_{H2} for the desorption reaction are determined. The desorption activation energy is confirmed by DSC measurements that show a shoulder after the main peak temperatures, which is concluded to origin from a bigger particle fraction that results from sintering and agglomeration after cycling the material. A higher activation energy will lead to a lower reaction rate regarding the temperature level of the system. This effect will have a lower overall impact since the main limiting parameter of the system remains the thermal conductance of the bed. As a crucial value for the overall performance of the tank system a modified model for the effective thermal conductivity is implemented, which considers partially sintered powder beds. Experiments in an autoclave with an enlarged powder mass are carried out under identic thermodynamic conditions as for the measurements in the Sieverts apparatus, but in scaled-up conditions of a tank system. From the medium scale experiments, important new insights are obtained, like the limitation of the kinetics by limited heat transfer, or the interaction between the pressure drop, caused by hydrogen flow, and the reaction behavior. These effects are not observable in lab-scale experiments. The geometry of the autoclave and the developed reaction model are implemented into a FEM simulation tool. Differences between the simulations and the experiments are identified, which, however, could be well justified like the unexpected turning point in the temperature development during the desorption reaction in the experiment that is not visible in the simulation results, due to a fixed pressure value. The conclusions drawn from the comparison of real experiments and predictive simulations help to develop a better understanding in view of system design. This work presents the first ever made model for the hydrogenation and dehydrogenation reaction of recycled Mg/Al-based waste on a medium scale system size. The simulation model is an approach for a method to predict even larger systems. Based on this, it can now be utilized for sensitivity analysis and to design tank systems for energy storage purposes for application scale.

Declaration of Competing Interest

The authors declare that there are no conflicts of interest.

Acknowledgments

The authors are thankful to Thomas Breckwoldt[b] from the Helmut-Schmidt University in Hamburg for the support with the SEM measurements.

Supplementary materials

Supplementary material associated with this article can be found, in the online version, at doi:10.1016/j.jma.2021.12.005.

References

[1] M. Wahlström, P. Kocyba, Vydt M.D. and J. Moor. Protest for a future: composition, mobilization and motives of the participants in Fridays For Future climate protests on 15 March 2019 in 13 European cities. Project Report; 2019.
[2] Regulation (EU) 2018/842 of the European parliament and of the council of 30 May 2018 on binding annual greenhouse gas emission reductions by member states from 2021 to 2030 contributing to climate action to meet commitments under the Paris agreement and amending regulation (EU) no 525/2013: PE/3/2018/REV/2, Off J Eur Union (2018) 26–42.
[3] A. Sgobbi, W. Nijs, M.R. de, A. Chiodi, M. Gargiulo, C. Thiel, How far away is hydrogen? Its role in the medium and long-term decarbonisation of the European energy system, Int J Hydrog Energy 41 (1) (2016) 19–35, doi:10.1016/j.ijhydene.2015.09.004.
[4] M. Hirscher, Handbook of hydrogen storage: new materials for future energy storage, Wiley-VCH, Weinheim, 2010.
[5] J. Bellosta von Colbe, J.R. Ares, J. Barale, M. Baricco, C. Buckley, G. Capurso, et al., Application of hydrides in hydrogen storage and compression: achievements, outlook and perspectives, Int J Hydrog Energy 44 (15) (2019) 7780–7808, doi:10.1016/j.ijhydene.2019.01.104.
[6] B. Sakintuna, F. Lamaridarkrim, M. Hirscher, Metal hydride materials for solid hydrogen storage: a review, Int J Hydrog Energy 32 (9) (2007) 1121–1140, doi:10.1016/j.ijhydene.2006.11.022.
[7] G. Capurso, B. Schiavo, J. Jepsen, G. Lozano, O. Metz, A. Saccone, et al., Development of a modular room-temperature hydride storage system for vehicular applications, Appl Phys A 122 (3) (2016) 3832, doi:10.1007/s00339-016-9771-x.
[8] H. Buchner, Energiespeicherung in metallhydriden, Vienna: Springer Vienna, 1982.
[9] D.A. Sheppard, M. Paskevicius, T.D. Humphries, M. Felderhoff, G. Capurso, J. Bellosta von Colbe, et al., Metal hydrides for concentrating solar thermal power energy storage, Appl Phys A 122 (4) (2016), doi:10.1007/s00339-016-9825-0.
[10] D.N. Harries, M. Paskevicius, D.A. Sheppard, T.E.C. Price, C.E. Buckley, Concentrating solar thermal heat storage using metal hydrides, Proc IEEE 100 (2) (2012) 539–549, doi:10.1109/JPROC.2011.2158509.
[11] M. Felderhoff, R. Urbanczyk, S. Peil, Thermochemical heat storage for high temperature applications – a review, Green 3 (2) (2013), doi:10.1515/green-2013-0011.
[12] B. Bogdanović, A. Ritter, B. Spliethoff, Active MgH_2/Mg systems for reversible chemical energy storage, Angew Chem Int Ed Engl 29 (3) (1990) 223–234, doi:10.1002/anie.199002233.
[13] M. Paskevicius, D.A. Sheppard, C.E. Buckley, Thermodynamic changes in mechanochemically synthesized magnesium hydride nanoparticles, J Am Chem Soc 132 (14) (2010) 5077–5083, doi:10.1021/ja908398u.
[14] P. Marty, J.F. Fourmigue, P.D. Rango, D. Fruchart, J. Charbonnier, Numerical simulation of heat and mass transfer during the absorption of hydrogen in a magnesium hydride, Energy Convers Manag 47 (20) (2006) 3632–3643, doi:10.1016/j.enconman.2006.03.014.
[15] Y. Shang, C. Pistidda, G. Gizer, T. Klassen, M. Dornheim, Mg-based materials for hydrogen storage, J Magnes Alloys 109 (2021) 103, doi:10.1016/j.jma.2021.06.007.
[16] V.A. Yartys, M.V. Lototskyy, E. Akiba, R. Albert, V.E. Antonov, J.R. Ares, et al., Magnesium based materials for hydrogen based energy storage: past, present and future, Int J Hydrog Energy 44 (15) (2019) 7809–7859, doi:10.1016/j.ijhydene.2018.12.212.
[17] M. Paskevicius, D.A. Sheppard, K. Williamson, C.E. Buckley, Metal hydride thermal heat storage prototype for concentrating solar thermal power, Energy 88 (2015) 469–477, doi:10.1016/j.energy.2015.05.068.
[18] M. Pęska, K. Smektalska, J. Dworecka-Wójcik, S. Terlicka, W. Gąsior, W. Gierlotka, et al., Hydrogen sorption behavior of mechanically synthesized Mg–Ag alloys, Int J Hydrog Energy 46 (66) (2021) 33152–33163, doi:10.1016/j.ijhydene.2021.07.120.
[19] A. Dębski, M. Pęska, J. Dworecka-Wójcik, S. Terlicka, W. Gąsior, W. Gierlotka, et al., Structural and calorimetric studies of magnesium-rich Mg-Pd alloys, J Alloys Compd 858 (2021) 158085, doi:10.1016/j.jallcom.2020.158085.
[20] W. Gierlotka, A. Dębski, S. Terlicka, W. Gąsior, M. Pęska, M. Polański, et al., Insight into phase stability in the Mg-Pt system. The Ab initio calculations, J Phase Equilib Diffus 42 (1) (2021) 102–106, doi:10.1007/s11669-020-00857-7.
[21] W. Gierlotka, A. Dębski, S. Terlicka, W. Gąsior, M. Pęska, M. Polański, Insight into phase stability in the Mg-Pd system: the Ab initio calculations, J Phase Equilib Diffus 41 (5) (2020) 681–686, doi:10.1007/s11669-020-00836-y.
[22] M. Pęska, T. Czujko, M. Polański, Hydrogenation ability of Mg-Li alloys, Energies 13 (8) (2020) 2080, doi:10.3390/en13082080.
[23] J.J. Reilly, R.H. Wiswall, Reaction of hydrogen with alloys of magnesium and nickel and the formation of Mg_2NiH_4, Inorg Chem 7 (11) (1968) 2254–2256, doi:10.1021/ic50069a016.
[24] J.J. Reilly, R.H. Wiswall, Reaction of hydrogen with alloys of magnesium and copper, Inorg Chem 6 (12) (1967) 2220–2223, doi:10.1021/ic50058a020.
[25] B. Bogdanovic, A process steam generator based on the high temperature magnesium hydride/magnesium heat storage system, Int J Hydrog Energy 20 (10) (1995) 811–822, doi:10.1016/0360-3199(95)00012-3.
[26] N. Bell, R. Waugh and D. Parker. Magnesium Recycling in the EU: Material flow Analysis of Magnesium (metal) in the EU and a Derivation of the Recycling Rate. Aylesbury, United Kingdom; 2017.
[27] European Commission. Critical raw materials profiles: report on critical raw materials for the eu; 2015.
[28] T.E. Graedel, J. Allwood, J.P. Birat, M. Buchert, C. Hagelüken, B.K. Reck, et al., What do we know about metal recycling rates? J Ind Ecol 15 (3) (2011) 355–366, doi:10.1111/j.1530-9290.2011.00342.x.
[29] T.D. Humphries, K.T. Møller, W.D.A. Rickard, M.V. Sofianos, S. Liu, C.E. Buckley, et al., Dolomite: a low cost thermochemical energy storage material, J Mater Chem A 7 (3) (2019) 1206–1215, doi:10.1039/c8ta07254j.
[30] A. Caraballo, S. Galán-Casado, Á. Caballero, S. Serena, Molten salts for sensible thermal energy storage: a review and an energy performance analysis, Energies 14 (4) (2021) 1197, doi:10.3390/en14041197.
[31] E. González-Roubaud, D. Pérez-Osorio, C. Prieto, Review of commercial thermal energy storage in concentrated solar power plants: steam vs. molten salts, Renew Sustain Energy Rev 80 (4) (2017) 133–148, doi:10.1016/j.rser.2017.05.084.
[32] Q. Peng, J. Ding, X. Wei, G. Jiang, Thermodynamic investigation of the eutectic mixture of the $LiNO_3$ - $NaNO_3$ - KNO_3 - $Ca(NO_3)_2$ system, Int J Thermophys 38 (9) (2017) 249, doi:10.1007/s10765-017-2284-9.
[33] M. Mehos, C. Turchi, J. Vidal, M. Wagner, M. Zhiwen, et al., Concentrating solar power Gen3 demonstration roadmap sandia National Laboratories, Alan Kruizenga: sandia National Laboratories (eds.), NREL, 2017 Technical ReportU.S. Department of Energy.
[34] W. Ding, A. Bonk, T. Bauer, Molten chloride salts for next generation CSP plants: selection of promising chloride salts & study on corrosion of alloys in molten chloride salts, in: Proceedings of the SolarPACES: international conference on concentrating solar power and chemical energy systems, AIP Publishing, 2019.
[35] D.F. Williams, K.T. Clarno, Evaluation of salt coolants for reactor applications, Nucl Technol 163 (3) (2008) 330–343, doi:10.13182/NT08-A3992.
[36] T. Wang, D. Mantha, R.G. Reddy, Novel high thermal stability LiF–Na_2CO_3–K_2CO_3 eutectic ternary system for thermal energy storage applications, Sol Energy Mater Sol Cells 140 (2015) 366–375, doi:10.1016/j.solmat.2015.04.033.
[37] M. Schmitz, Rohstoffrisikobewertung - magnesium (metall), Berlin: Deutsche Rohstoffagentur (DERA) in Der Bundesanstalt für Geowissenschaften Und Rohstoffe (BGR), 2019 2018th ed..

[38] C. Pistidda, N. Bergemann, J. Wurr, A. Rzeszutek, K.T. Møller, B.R.S. Hansen, et al., Hydrogen storage systems from waste Mg alloys, J Power Sources 270 (2014) 554–563, doi:10.1016/j.jpowsour.2014.07.129.
[39] R. Hardian, C. Pistidda, A.L. Chaudhary, G. Capurso, G. Gizer, H. Cao, et al., Waste Mg-Al based alloys for hydrogen storage, Int J Hydrog Energy 43 (34) (2018) 16738–16748, doi:10.1016/j.ijhydene.2017.12.014.
[40] Y. Li, Y. Zhang, H. Shang, Y. Qi, P. Li, D. Zhao, Investigation on structure and hydrogen storage performance of as-milled and cast $Mg_{90}Al_{10}$ alloys, Int J Hydrog Energy 43 (13) (2018) 6642–6653, doi:10.1016/j.ijhydene.2018.02.086.
[41] A. Andreasen, Hydrogenation properties of Mg–Al alloys, Int J Hydrog Energy 33 (24) (2008) 7489–7497, doi:10.1016/j.ijhydene.2008.09.095.
[42] S. Bouaricha, J.P. Dodelet, D. Guay, J. Huot, S. Boily, R. Schulz, Hydriding behavior of Mg–Al and leached Mg–Al compounds prepared by high-energy ball-milling, J Alloys Compd 297 (1–2) (2000) 282–293, doi:10.1016/S0925-8388(99)00612-X.
[43] J.C. Crivello, T. Nobuki, S. Kato, M. Abe, T. Kuji, Hydrogen absorption properties of the -$Mg_{17}Al_{12}$ phase and its Al-richer domain, J Alloys Compd 446-447 (2007) 157–161, doi:10.1016/j.jallcom.2006.12.055.
[44] J.C. Crivello, T. Nobuki, T. Kuji, Improvement of Mg–Al alloys for hydrogen storage applications, Int J Hydrog Energy 34 (4) (2009) 1937–1943, doi:10.1016/j.ijhydene.2008.11.039.
[45] J. Atilio Puszkiel, M. Rahman, Tailoring the kinetic behavior of hydride forming materials for hydrogen storage, Gold nanoparticles: reaching new heights, IntechOpen, London, 2019.
[46] L.F. Jones, D. Dollimore, T. Nicklin, Comparison of experimental kinetic decomposition data with master data using a linear plot method, Thermochim Acta 13 (2) (1975) 240–245, doi:10.1016/0040-6031(75)80085-2.
[47] J.H. Sharp, G.W. Brindley, B.N.N Achar, Numerical data for some commonly used solid state reaction equations, J Am Ceram Soc 49 (7) (1966) 379–382, doi:10.1111/j.1151-2916.1966.tb13289.x.
[48] J.F. Fernández, C.R. Sánchez, Rate determining step in the absorption and desorption of hydrogen by magnesium, J Alloys Compd 340 (1–2) (2002) 189–198, doi:10.1016/S0925-8388(02)00120-2.
[49] P.S. Rudman, Hydrogen-diffusion-rate-limited hydriding and dehydriding kinetics, J Appl Phys 50 (11) (1979) 7195–7199, doi:10.1063/1.325831.
[50] M.H. Mintz, Z. Gavra, G. Kimmel, Z. Hadari, The reaction of hydrogen with magnesium alloys and magnesium intermetallic compounds, J Less Common Met 74 (2) (1980) 263–270, doi:10.1016/0022-5088(80)90161-7.
[51] A. Karty, J. Grunzweig-Genossar, P.S. Rudman, Hydriding and dehydriding kinetics of Mg in a Mg/Mg_2Cu eutectic alloy: pressure sweep method, J Appl Phys 50 (11) (1979) 7200–7209, doi:10.1063/1.325832.
[52] F.H. Ellinger, C.E. Holley, B.B. McInteer, D. Pavone, R.M. Potter, E. Staritzky, et al., The preparation and some properties of magnesium hydride, J Am Chem Soc 77 (9) (1955) 2647–2648.
[53] J.S. Han, M. Pezat, L. Jai-Young, A study of the decomposition of magnesium hydride by thermal analysis, J Less Common Met 130 (1987) 395–402, doi:10.1016/0022-5088(87)90134-2.
[54] A. Andreasen, T. Vegge, A.S. Pedersen, Compensation effect in the hydrogenation/dehydrogenation kinetics of metal hydrides, J Phys Chem B 109 (8) (2005) 3340–3344, doi:10.1021/jp0458755.
[55] J. Huot, G. Liang, S. Boily, A. van Neste, R. Schulz, Structural study and hydrogen sorption kinetics of ball-milled magnesium hydride, J Alloys Compd 293-295 (1999) 495–500, doi:10.1016/S0925-8388(99)00474-0.
[56] A. Khawam, D.R. Flanagan, Solid-state kinetic models: basics and mathematical fundamentals, J Phys Chem B 110 (35) (2006) 17315–17328, doi:10.1021/jp062746a.
[57] A.M. Ginstling, B.I. Brounshtein, Concerning the diffusion kinetics of reactions in spherical particles, J Appl Chem USSR 23 (12) (1950) 1327–1338.
[58] W. Jander, Reaktionen im festen zustande bei höheren temperaturen. Reaktionsgeschwindigkeiten endotherm verlaufender umsetzungen, Z Anorg Allg Chem 163 (1) (1927) 1–30, doi:10.1002/zaac.19271630102.
[59] H.T. Uchida, S. Wagner, M. Hamm, J. Kürschner, R. Kirchheim, B. Hjörvarsson, et al., Absorption kinetics and hydride formation in magnesium films: effect of driving force revisited, Acta Mater 85 (2015) 279–289, doi:10.1016/j.actamat.2014.11.031.
[60] C.M. Stander, Kinetics of decomposition of magnesium hydride, J Inorg Nucl Chem 39 (2) (1977) 221–223, doi:10.1016/0022-1902(77)80003-1.
[61] W. Oelerich, R. Bormann, V. Güther Sorptionseigenschaften von nanokristallinen Metallhydriden für die Wasserstoffspeicherung.
[62] G. Barkhordarian, T. Klassen, R. Bormann, Kinetic investigation of the effect of milling time on the hydrogen sorption reaction of magnesium catalyzed with different Nb_2O_5 contents, J Alloys Compd 407 (1–2) (2006) 249–255, doi:10.1016/j.jallcom.2005.05.037.
[63] J.F. Fernández, C.R. Sánchez, Simultaneous TDS–DSC measurements in magnesium hydride, J Alloys Compd 356-357 (2003) 348–352, doi:10.1016/S0925-8388(02)01228-8.
[64] G.A. Lozano, J.M. Bellosta von Colbe, T. Klassen, M. Dornheim, Transport phenomena versus intrinsic kinetics: hydrogen sorption limiting sub-process in metal hydride beds, Int J Hydrog Energy 39 (33) (2014) 18952–18957, doi:10.1016/j.ijhydene.2014.09.035.
[65] A. Chaise, P.D. Rango, P. Marty, D. Fruchart, Experimental and numerical study of a magnesium hydride tank, Int J Hydrog Energy 35 (12) (2010) 6311–6322, doi:10.1016/j.ijhydene.2010.03.057.
[66] P. Zehner, E.U. Schlünder, Wärmeleitfähigkeit von schüttungen bei mäßigen temperaturen, Chem Ing Tech 42 (14) (1970) 933–941, doi:10.1002/cite.330421408.
[67] P. Zehner, E.U. Schlünder, Einfluß der wärmestrahlung und des druckes auf den wärmetransport in nicht durchströmten schüttungen, Chem Ing Tech 44 (23) (1972) 1303–1308, doi:10.1002/cite.330442305.
[68] V.D. Ingenieure, VDI-gesellschaft verfahrenstechnik und chemieingenieurwesen, VDI-wärmeatlas: Mit 320 tabellen, 11th ed., Springer Vieweg, Berlin, 2013.
[69] M. Bortz, B. Bertheville, G. Böttger, K. Yvon, Structure of the high pressure phase γ-MgH_2 by neutron powder diffraction, J Alloys Compd 287 (1–2) (1999) L4–L6, doi:10.1016/S0925-8388(99)00028-6.
[70] J.C. Crivello, B. Dam, R.V. Denys, M. Dornheim, D.M. Grant, J. Huot, et al., Review of magnesium hydride-based materials: development and optimisation, Appl Phys A 122 (2) (2016) 5077, doi:10.1007/s00339-016-9602-0.
[71] A. Sanchez, Expanded graphite as heat transfer matrix in metal hydride beds, Int J Hydrog Energy 28 (5) (2003) 515–527, doi:10.1016/S0360-3199(02)00057-5.
[72] D.A. Mosher, X. Tang, R.J. Brown, S. Arsenault, S. Saitta, B.L. Laube et al. High density hydrogen storage system demonstration using NaAlH4 based complex compound hydrides.
[73] D.E. Dedrick, M.P. Kanouff, B.C. Replogle, K.J. Gross, Thermal properties characterization of sodium alanates, J Alloys Compd 389 (1–2) (2005) 299–305, doi:10.1016/j.jallcom.2004.08.007.
[74] F. Richter. Die physikalischen eigenschaften der stähle "das 100 - stähle - programm": teil i: tafeln und bilder. Mülheim a.d. Ruhr.
[75] C. PC. Flow of gases through porous media 1956.
[76] J. Kapischke, J. Hapke, G. Brunner, Entwicklung und untersuchung einer startvorrichtung zur aktivierung eines hochtemperaturhydridreaktors, in: Arbeitsbereich Verfahrenstechnischer Apparatebau, Hamburg-Harburg, Technology University, Düsseldorf: VDI-Verl, 1996, p. 1996. Zugl.Diss.
[77] B. Delhomme, M.P. Rango P de, M. Bacia, B. Zawilski, C. Raufast, et al., Large scale magnesium hydride tank coupled with an external heat source, Int J Hydrog Energy 37 (11) (2012) 9103–9111, doi:10.1016/j.ijhydene.2012.03.018.